PAPER

Check for updates

CoP-nanorod-doped Co heterostructured electrode for efficient electrocatalytic hydrogen evolution reaction

Yuanze Wei, [ID] Shiyu Yang, Danyang Yu, Zhifan Xue and Benxue Zou [ID] *

A high-performance CoP-nanorod doped Co metal on Ni foam (CoP/Co/NF) electrocatalytic electrode was designed *via* a two-step strategy involving electrodeposition and low-temperature phosphorization. The heterogeneous structures of metallic Co and CoP on the Ni foam are expected to provide hierarchical interfaces, which promote the synergistic effect in the electrocatalysis process. The electrode surface shows a hierarchical architecture of sea-urchin-like arrays directly grown on conductive substrates with a large electrochemical active surface area (ECSA) of 537.5 cm^2, which facilitate rapid bubble release and ensure stable low-energy operation even at high current densities. Electrochemical test results show that the CoP/Co/NF catalyst electrode exhibits an excellent catalytic activity for the hydrogen evolution reaction in 1 M KOH electrolyte. The optimized overpotential reached 23 and 56 mV at a current density of 10 and 100 mA cm^{-2} with a low Tafel slope of 27.1 mV dec^{-1}. The electrode shows good stability after catalytic hydrogen evolution reaction for 100 h at 100 mA cm^{-2}. Theoretical DFT calculations reveal that the CoP/Co interface serves as an electron-rich center that lowers the energy barrier for water dissociation and optimizes ΔG_{H*}.

1 Introduction

Currently, the greenhouse effect has driven the global average temperature to a critical threshold, which will trigger irreversible changes in the global ecosystem. The primary root cause of the greenhouse effect lies in the excessive exploitation and utilization of traditional fossil fuels, such as coal, oil, and natural gas. Hydrogen, distinguished by its high gravimetric energy density and zero-carbon emission profile, is universally recognized as the cornerstone of future decarbonized energy systems, particularly for hard-to-abate sectors such as steel manufacturing and heavy transport.[1–3] Among the various hydrogen production technologies, water electrolysis is a green and environmentally friendly method that directly decomposes water to produce high-purity hydrogen, which is independent of traditional fossil fuels. Proton exchange membrane (PEM) water electrolysis offers rapid response and high current densities; its mass deployment is severely constrained by the scarcity and exorbitant cost of iridium and platinum group metals (PGMs). Alkaline water electrolysis (AWE) remains the predominant industrial standard for large-scale hydrogen production. However, the widespread efficiency of AWE is currently hampered by the sluggish kinetics of the Hydrogen evolution reaction (HER) in alkaline media. Unlike in acidic environments, alkaline HER involves an additional, energy-intensive

Department of Chemical Engineering, Liaodong University, Dandong, 118001, China. E-mail: zoubenxue@liaodongu.edu.cn

water dissociation step (H$_2$O + e$^-$ → H* + OH$^-$), which imposes a substantial activation energy barrier (Volmer step) and high overpotentials.[4–7] Noble metal catalysts are still considered the state-of-the-art electrocatalysts for water electrolysis owing to their ultra-high electrical conductivity and favorable H* adsorption and H$_2$ desorption capabilities. However, their high cost and poor long-term stability prevent their large-scale production. Therefore, developing cost-effective electrocatalysts with optimal water dissociation efficiency and hydrogen adsorption energetics is the critical bottleneck for the hydrogen economy.

Transition metal catalysts including transition metal oxides (TMOs), nitrides (TMNs), sulfides (TMS), phosphides (TMPs), carbides and selenides have become crucial objectives in HER catalyst research.[8–13] TMPs, particularly cobalt phosphides (CoP), have emerged as front-runners to replace platinum due to their metalloid characteristics and the unique "ensemble effect", wherein negatively charged phosphorus centers act as effective proton acceptors.[14–16] Despite their promise, single-phase CoP catalysts often suffer from suboptimal water adsorption capabilities and moderate electronic conductivity, which restrict their catalytic performance and stability under industrial-grade high current densities. Various modification strategies, such as heteroatom doping, defect engineering, and heterostructure construction, have been employed to enhance its performance. For instance, Liu *et al.* proposed a HER catalyst based on a nickel foam substrate with Fe doped into CoP (Fe-CoP/NF), which demonstrated significantly improved

performance compared to pristine CoP.[15] This enhancement was attributed to the regulation of the electron density around Co atoms by the introduced Fe, resulting in more active sites and thus enhanced reaction activity. Liu *et al.* utilized the introduction of a pure metallic Co phase to improve the efficiency of electron transfer within the catalyst.[16] They developed a highly efficient overall water-splitting catalyst with an HER overpotential of only 78 mV@10 mA cm^{-2} in alkaline media by optimizing the hydrogen adsorption free energy (ΔG_{H*}). Wang *et al.* employed a method involving hydrothermal treatment followed by high-temperature phosphidation to incorporate CoP into a NiP system, forming a heterostructured catalyst (CoP/NiP).[17] Through density functional theory (DFT) calculations, they concluded that NiP acts as an 'electron pump' for CoP, facilitating interfacial electron transfer. Owing to the synergistic effects of the catalyst's microstructure and unique interfacial electronics, the H* adsorption/H$_2$ desorption at the CoP/NiP heterointerface was optimized, reducing the HER energy barrier and endowing the catalyst with high HER activity.

Recent theoretical and experimental breakthroughs suggest that heterostructure engineering can effectively modulate the electronics, active sites, adsorption/desorption free energy, and activation energy within the catalyst. The formation of a Mott–Schottky interface between a metal and a semiconductor can induce a built-in electric field (BIEF), triggering interfacial electron redistribution that optimizes the d-band center of active sites.[18] Specifically, metallic cobalt (Co) or iron (Fe) can function as an "electron pump", donating electrons to the TMPs phase to enhance intrinsic conductivity and modulate the Gibbs free energy of hydrogen adsorption toward thermo-neutrality, thereby synergistically lowering the kinetic barrier for water cleavage. Beyond intrinsic electronic modulation, the macroscopic morphology of the electrode plays a pivotal role in mass transport, particularly at high current densities where gas bubble accumulation can block active sites and induce severe ohmic losses. Three-dimensional (3D) hierarchical architectures, such as sea-urchin-like arrays directly grown on conductive substrates, offer a dual advantage: they maximize the electrochemically active surface area (ECSA) and create "superhydrophilic" surfaces that facilitate rapid gas bubble detachment, ensuring continuous electrolyte-catalyst contact.[19,20] Although various CoP-based catalysts have been reported, the synergistic coupling of metallic Co nanorods with CoP in a cohesive, binder-free 3D architecture to simultaneously tackle the kinetic barrier of water dissociation and the hydrodynamic challenge of gas release remains relatively underexplored.

Herein, we fabricated a high-performance heterostructured electrocatalyst comprising CoP nanorods doped with metallic Co, anchored on nickel foam (CoP/Co/NF), *via* a facile electrodeposition followed by a controlled low-temperature phosphorization strategy. This heterogeneous design leverages the synergistic interaction between metallic Co and CoP to create hierarchical interfaces that significantly enhance electrocatalytic activity. Density functional theory (DFT) calculations reveal that the CoP/Co interface serves as an electron-rich center that lowers the energy barrier for water dissociation and

optimizes ΔG_{H*}. The unique sea-urchin-like morphology provides abundant active sites and facilitates rapid bubble release. Consequently, the CoP/Co/NF electrode exhibits exceptional HER performance with an ultralow overpotential of 23 and 56 mV at 10 mA cm^{-2} and 100 mA cm^{-2}, and outstanding long-term stability in alkaline media, positioning it as a robust candidate for next-generation advanced alkaline water splitting.

2 Experimental section

2.1 Preparation of CoP/Co/NF

Prior to the deposition of metallic Co, nickel foam (NF) was immersed in acetone for 3 minutes, rinsed with distilled water and air dried for later use. Two-electrode system was used to electrodeposite the metallic Co by chronopotentiometry technique (CP) in 0.1 M CoCl$_2$ and 2 M NH$_4$Cl electrolyte with Ni foam as the working electrode and a carbon rod as the counter electrode. The electrodeposition was performed at a constant current density with a geometric deposition area of 0.5 × 0.5 cm^2. The obtained Co-modified film on Ni foam (Co/NF) was then washed with deionized water and dried in air at room temperature. Subsequent phosphorization was carried out with 1 g NaH$_2$PO$_2$·H$_2$O on the upstream of the quartz boat at 400 °C for 2 h under 20 SCCM N$_2$ flow with a temperature increase rate of 5 °C min^{-1}. The obtained sample was denoted as CoP/Co/NF. For comparison, CoP/Co/NF-*x* (abbreviated as CoP-*x*) were obtained by varying electro-deposition current from 0.10 A to 0.25 A, deposition time (300–600 s) and phosphorization time (40–160 min). To illustrate the advantage of CoP/Co/NF, the CoP directly grown on the Ni foam without using metallic Co precursor (denoted as CoP/NF) was prepared according to the ref. 21.

2.2 Characterization

The morphology and elemental composition of the samples were studied by field-emission scanning electron microscopy (SEM, Carl Zeiss, Germany) and JEOL-2100F FETEM transmission electron microscopy (TEM). The composition was determined by X-ray photoelectron spectra (XPS) on Thermo ECSALAB 250 electron spectrometer using Al Kα radiation. X-ray diffraction (XRD) patterns were collected by an X-ray diffractometer (XRD, PANalytical B.V., Thermo Scientific, Netherlands). Electrochemical measurements were performed on a CHI660e potentiostat using a three-electrode system with a carbon rod as counter electrode and Hg/HgO (1.0 M KOH) as reference electrode. Electrocatalystic performances of the electrodes were evaluated by linear sweep voltammetry (LSV), cyclic voltammetry (CV), chronopotentiometry (CP) and electrochemical impedance spectroscopy (EIS) with 1.0 M KOH electrolyte as the electrolyte. To eliminate the influence of ohmic impedance to reveal the intrinsic catalytic properties, the potential was calibrated to the reversible hydrogen electrode (RHE) value with *iR* correction according to the following equation:

$$E_{HER} = E_{Hg/HgO} + 0.059 \times pH + 0.098 - iR$$

LSV tests were conducted with 75% *iR* compensation. Electrochemical surface areas (ECSA) were evaluated using a series of CV curves between 0.25 V and 0.35 V *vs.* the RHE at scan rates of 20, 40, 60, 80, 100, 120, 140, 160, and 180 mV s^{-1}. The number of active site (N) was measured by cyclic voltammetry measurements in pH 6.86 phosphate buffer at a scan rate of 50 mV s^{-1}.[22] The N of the catalyst can be calculated using the following equation:

$$N = \frac{Q}{2 \times F}$$

where Q is the voltammetric charge calculated by integrated area of the CV curve minus the blank area, F is the Faraday constant (96 485.3 C mol^{-1}). The turnover frequency (TOF) of the catalyst is calculated by the formula:

$$\text{TOF} = j/2 \times F \times N$$

where j is the current density given by the LSV measurements at overpotential of 100 mV in 1M KOH and N is the number of active sites of the electrode. EIS spectra were measured at frequency range at -0.2 V *vs.* RHE from 100 kHz to 10 mHz with potential amplitude of 5 mV.

2.3 Theoretical calculation

DFT calculations were conducted using the materials studio (MS) with CASTEP calculation module. Moreover, the exchange-correlation between electrons was characterized using generalized gradient approximation (GGA) and Perdew–Burke–Ernzerhof (PBE) functions. The cutoff energy for plane waves was set at 600 eV, with a $3 \times 3 \times 3$ Monkhorst–Pack k-point grid sampling the Brillouin zone. To avoid interaction from other planes, we used 15 Å the vacuum layer thickness. The optimization criteria for the model structure's energy and force convergence were established at 2×10^{-4} eV and 0.05 eV Å^{-1}, respectively. The optimized structure model for DFT calculation was derived

from XRD data, and the CoP/Co heterojunction structure model was constructed by connecting CoP crystal (111) plane to Co crystal (111) plane. For comparison, pristine CoP and Co models were established, aligning with their respective (111) and (111) crystal planes. Gibbs energy for the adsorption of hydrogen can be calculated as the follow formula:

$$\Delta G_{H^*} = \Delta E_{H^*} + \Delta E_{ZPE} - T\Delta S$$

where, ΔE_{H^*} represents the energy change associated with the binding of an H atom at the adsorption location, ΔE_{ZPE} is the zero-point energy correction, T is the room temperature (298.15 K), ΔS is the entropy change.[23] Similarly, the formula for $\Delta G_{H_2O^*}$ is as follows:

$$\Delta G_{H_2O^*} = E_{(H_2O^*)} - E_{(*)} - E_{(H_2O)} + \Delta E_{ZPE} - T\Delta S$$

where $E_{(H_2O^*)}$ is the total energy of water molecules adsorbed at the active site, $E_{(*)}$ is the total energy of the active site, and $E_{(H_2O)}$ represents the overall energy of an individual water molecule.

3 Results and discussion

3.1 Structural and morphological characterization

The fabrication route of the three dimensional hierarchical CoP-nanorods/Co/NF is illustrated in Fig. 1 The three-dimensional (3D) Ni foam was used as the substrate to provide a conductive surface for the deposition of the porous metallic Co film by electrochemical method. Subsequently, Co-precursors are partially converted to CoP nanorods by a low-temperature phosphorization process. The morphology and elemental distribution of the sample are characterized by scanning electron microscopy. Fig. 2 shows the SEM photos and EDS spectrum of the CoP/Co-modified electrode. The three-dimensional reticular pore structure of the modified film is clearly seen from the SEM image. These porous structures arise from the water molecules hydrolyzed to evolve hydrogen gas at
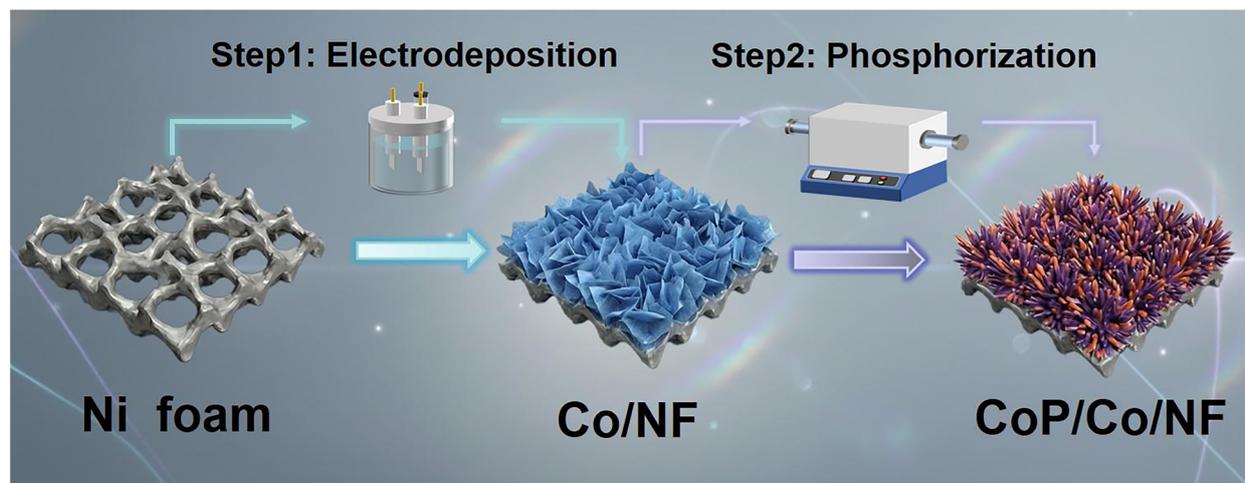

Fig. 1 Schematic diagram of the synthesis of the CoP-nanorods/Co/NF electrocatalyst.
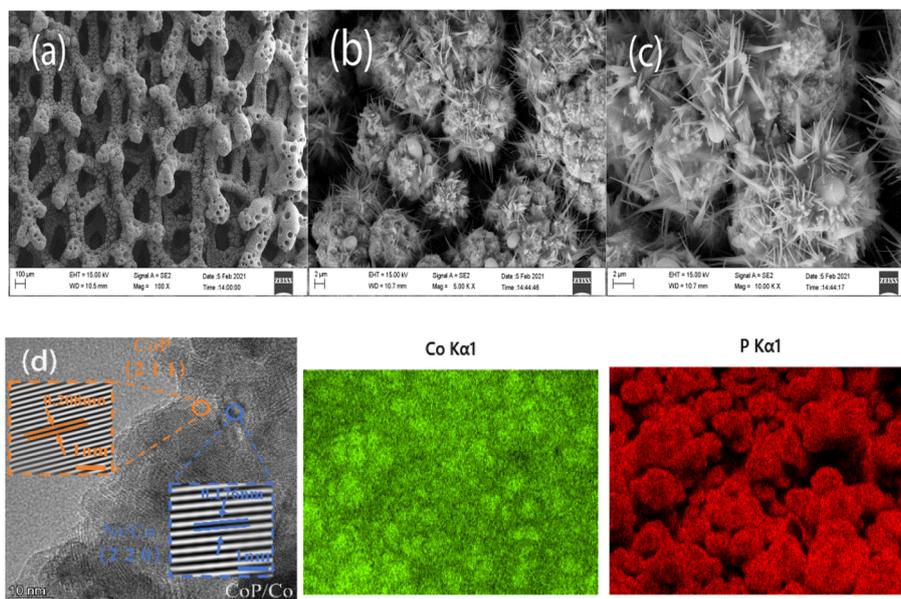
Fig. 2 (a–c) SEM images of CoP/Co/NF with different magnifications; (d) TEM images of CoP/Co/NF and (e and f) EDX elemental mapping of Co and P of CoP/Co/NF.

the electrode surface during the deposition of metal Co. The SEM images reveal the hierarchical architectures of sea-urchin-like arrays directly grown on conductive substrates. This sea urchin-like structure radiates countless nano-needles/rods outward from its center. Compared to smooth films or micro-particles, this open-topology structure significantly increases the specific surface area. This means that when outputting the same total current, the local current density on each active site is lower, thereby reducing the local overpotential requirement

and extending the catalyst lifespan. The sea urchin-like nano-needle array creates a rough surface with micro-nano composite structures. These structures facilitate exposure of more active catalytic sites for rapid gas bubble detachment, ensuring continuous electrolyte-catalyst contact, thus enhancing the catalytic activity for water splitting reaction.[24]

From the EDS surface spectrum, it can be seen that the nickel foam is uniformly distributed with the molecule ratio about 1.6 : 1 for Co and P elements, indicating partial Co
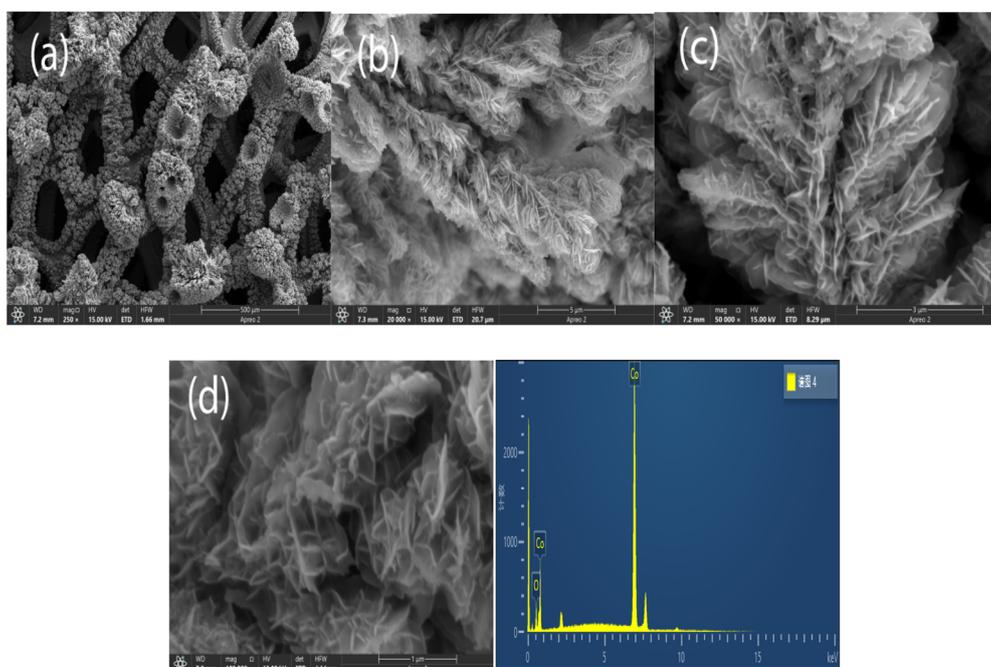

Fig. 3 (a–d) SEM images of Co precursors/NF with different magnifications and the corresponding EDX elemental mapping of Co on the Ni foam.

element on the electrode were phosphorized to form abundant heterostructures of the catalyst electrode. The multiple interfaces between CoP, Co and Ni foam can effectively regulate the d-band center and electronic structure of Co, meanwhile increase the number of reactive sites and improve the HER activity of catalysts. The SEM images and EDS spectrum of the firstly electrodeposited metallic Co precursors on the Ni foam were also shown in Fig. 3 The images exhibit the micrometer-sized seaweed-liked clusters constructed with a large number of nanosheets on its surface. This hierarchical architecture provides a significantly more specific surface area for the following formation of heterostructured CoP on the metallic Co. The EDS elemental mapping reveals the existence of Co (94.4%) and O (5.5%) atom, demonstrating the successful deposition of the metal Co on the Ni foam.

XRD is used to identify the composition and crystal structure of the catalyst. As shown in Fig. 4a, the XRD pattern of the prepared CoP/Co/NF shows Co_2P (DB card no. 9009202) with the diffraction peaks at 44.5°, 51.9° and 76.5°, which can be assigned to the crystal faces of (111), (200) and (220) for the Co_2P material.[23] The cobalt is typically considered to be near zero-valent or slightly positively charged (δ^+, $0 < \delta < 1$) in Co_2P, exhibiting a metallic bond with strong covalent characteristics. X-ray photoelectron spectroscopy (XPS) was further used to characterize the composition and electronic structure of the sample. The XPS spectra Fig. 4b shows characteristic peaks at around 140, 530 and 810 eV, corresponding to the P 2p, O 1s, and Co 2p regions, respectively. The presence of oxygen species could result from superficial oxidation of cobalt phosphide in air. In the XPS spectrum of Co 2p for the CoP/Co/NF Fig. 4c, the spin coupling of Co 2p were deconvoluted into 781.4 eV and

797.8 eV, corresponding to the Co $2p_{3/2}$ and Co $2p_{1/2}$.[24,25] Note that the integral area of Co $2p_{1/2}$ was almost half of the area corresponding to Co $2p_{3/2}$. The intense satellite peaks in Co 2p spectra observed at 786.7 and 802.7 eV can be ascribed to shake up excitation of the high-spin Co^{2+} ions in the sample. There observed small peak at 778.0 eV which can be ascribed to metallic Co, suggesting the existence of Co metal in the composite.[26] All spin coupling peaks shift to higher binding energies after phosphorization process, compared with those of Co 2p for the metallic Co precursors on the NF Fig. 4d, indicating the introduction of negative P atom leads to electron deficiency in metallic cobalt, which may facilitate the adsorption of the H_2O molecules on the catalyst. The high resolution XPS spectrum of P 2p shown in Fig. 4f, the spin–orbit peak at 129.8 eV can be ascribed to P$2p_{3/2}$ (Co–P bond) and peak at 134.0 eV ascribed to oxidized phosphorus (P–O), respectively.[27,28] From the high resolution of XPS of Co 2p core level, the metallic Co^0 content is calculated about 8.6 at% from the integral area of peak at 778.0 eV, Co^{2+} (e.g. Co–P) is about 51.1% and Co^{3+} (e.g. Co_3O_4, Co–P–O) at 783.3 eV is about 40.4%.

3.2 Catalytic hydrogen evolution performance test in alkaline electrolyte

3.2.1 Effect of deposition time and deposition current on hydrogen evolution performance.
Linear sweep voltammetry (LSV) was used to test the catalytic activity of the catalyst for the hydrogen evolution reaction. All potentials were relative to the standard hydrogen electrode (RHE), and the current densities were calculated on the basis of the geometric surface areas of electrodes. The LSV testing of hydrogen evolution catalysts
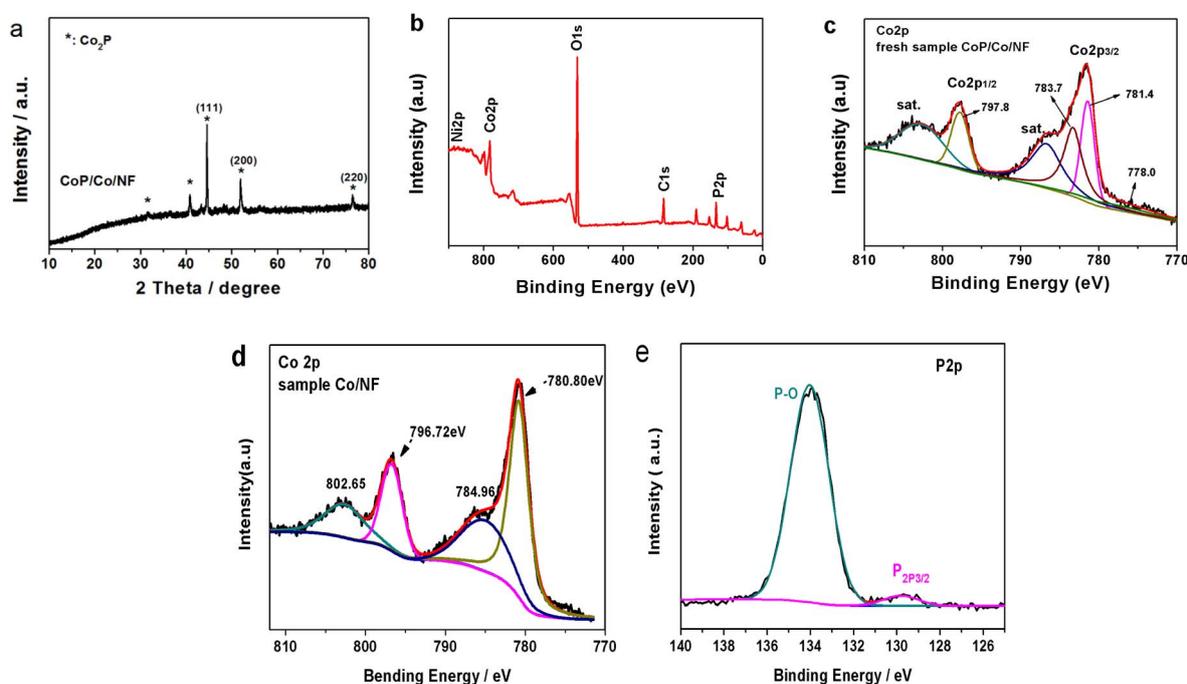

Fig. 4 (a) XRD patterns, (b) survey XPS spectrum and (c–e) high-resolution XPS spectra of Co 2p and P 2p for the CoP/Co/NF electrocatalyst and Co 2p for the Co precursors/NF.
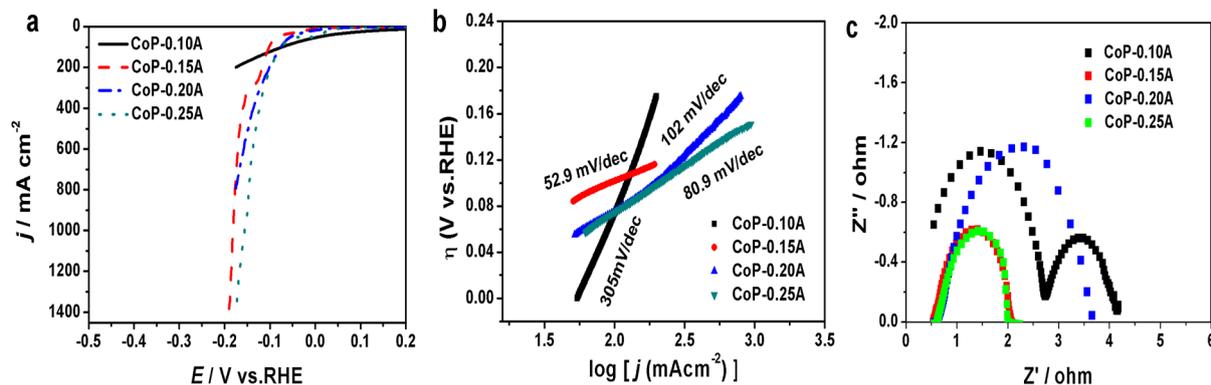
Fig. 5 (a) LSV hydrogen evolution polarization curves of CoP/Co/NF prepared at different current densities, scanning rate: 2 mV s^{-1}; (b) Tafel curves and slopes of CoP/Co/NF prepared at different current densities. (c) AC impedance spectra of CoP/Co/NF electrodes at −0.2 V vs. RHE.

requires appropriate *iR* compensation to eliminate the voltage drop caused by solution resistance (R_s). This ensures that the true overpotential reflects the intrinsic electrochemical performance of the catalyst. The polarization curves were carried out at a low scan rate of 2 mV s^{-1} using the online 75% *iR* compensation. The observed curve was smooth and oscillation-free. As shown in the Fig. 5a, CoP/Co/NF catalysts prepared under different deposition currents showed good electro-catalytic activity for the HER. The over-potential (η) of the CoP-0.15 A catalyst electrode exhibits superior over-potential (η) of 40 mV to reach current density of 10 mA cm^{-2}, lower than that of the CoP-0.25 A, CoP-0.20 A and CoP-0.10 A. The CoP-0.15 A catalyst electrode shows an overpotential of 120 mV to produce high current density of 100 mA cm^{-2}.

Fig. 5b shows the Tafel curves of the catalysts based on their respective polarization curves. The Tafel slope of CoP-0.15 A (52.9 mV dec^{-1}) is significantly lower than those catalysts, indicating that CoP-0.15 A provides higher catalytic kinetics and hydrogen production rate for the HER. Impedance technology was used to test the reaction resistance of the catalyst-modified electrode. The test voltage was applied as −0.2 V vs. HRE. As shown in the Fig. 5c, the frequency response of the CoP/Co/NF electrode is approximately semicircular, and the radius of the semicircle represents the charge transfer resistance R_{ct}. From

the AC impedance diagram, it can be seen that the reaction resistance of the CoP-0.15 A catalyst electrode was 1.5 Ω at a voltage of −0.2 V, lower than that of the catalysts prepared at other current densities, suggesting the higher conductivity of the catalyst and improved kinetic rate of the HER, which is consistent with the result of LSV.

The effect of deposition time on catalyst activity was also examined. The experimental results show that the catalyst samples obtained by deposition for 400 s and 500 s show better hydrogen evolution catalytic performances (Fig. 6a and b). From the AC impedance diagram Fig. 6c, the CoP-500 s catalyst electrode exhibits the smallest reaction resistance compared with the other samples. The optimized electro-deposition condition (0.15 A cm^{-2}, 500 s) is crucial as it determines the formation of the sea urchin-like nanoneedle morphology in the precursor. This binder-free growth method ensures strong ohmic contact between the catalyst and the substrate, thus reduces the contact resistance for the HER.

3.2.2 Effect of phosphorization time on hydrogen evolution performance. Controlling the degree of phosphorization is a key factor for ensuring the formation of the highly active CoP phase while retaining a portion of the metallic Co. This hierarchical structure not only preserves the high activity of CoP but also leverages the high conductivity of the metallic Co. The
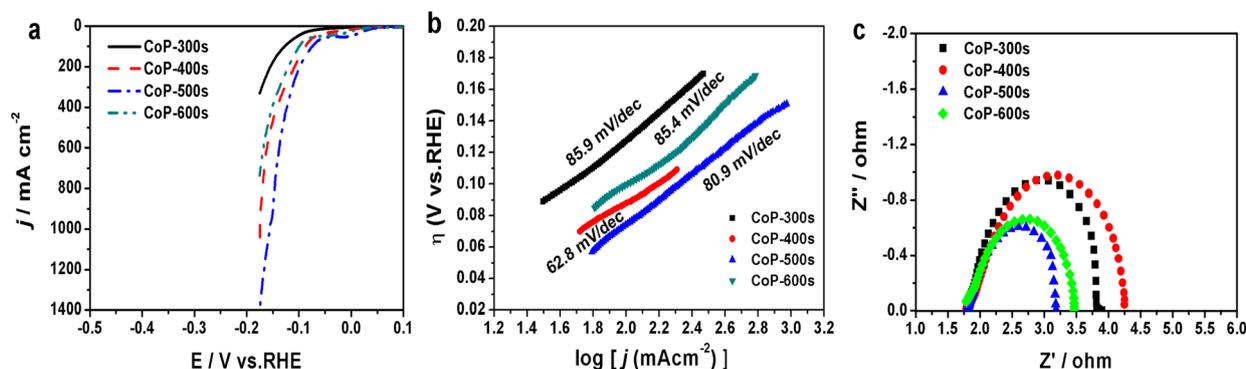

Fig. 6 (a) LSV hydrogen evolution polarization curves; (b) Tafel slopes; and (c) AC impedance spectra of CoP/Co/NF prepared at different deposition times.
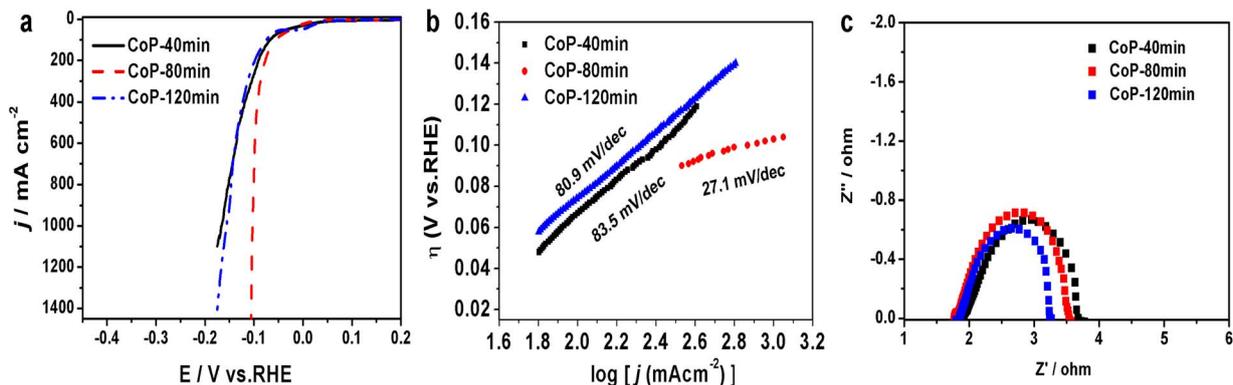
Fig. 7 (a) LSV hydrogen evolution polarization curves; (b) Tafel curves and slopes and (c) AC impedance spectra of CoP/Co/NF prepared at different phosphorization times.

effect of phosphorization time on catalyst activity was examined. The experimental results indicate that the degree of phosphidation has a significant impact on catalytic performance. When the phosphidation time is 80 min, the catalytic activity reaches its maximum. The catalyst sample CoP-80 min shows the best hydrogen evolution catalytic performance with the over-potential (η) of 23 mV to reach current density of 10 mA cm^{-2} (Fig. 7a and b). The Tafel slope of CoP-80 min is 27.1 mV dec^{-1}, significantly lower than those of CoP-40 min (83.5 mV dec^{-1}) and CoP-120 min (80.9 mV dec^{-1}), which indicates faster kinetics and a higher hydrogen generation rate during the HER process. From the AC impedance diagram shown in Fig. 7c, the

reaction resistance of the CoP-80 min catalyst electrode was 1.7 Ω, comparable with those of the catalysts. The mechanism of the HER in alkaline media is typically treated as a three elementary steps: first the Volmer reaction, that is, the water decomposition reaction and the formation of a reactive intermediate H_{ads} ($H_2O + e^- \rightarrow H_{ads} + OH^-$) with Tafel slope about 120 mV dec^{-1}; followed by Heyrovsky reaction ($H_{ads} + e^- + H_2O \rightarrow H_2 + OH^-$) and Tafel reaction ($H_{ads} + H_{ads} \rightarrow H_2$) with Tafel slope about 30–40 mV dec^{-1}.[9,10] The Tafel slope of the CoP-80 min electrode demonstrates the hydrogen evolution reaction of this electrode is kinetically controlled by the Tafel reaction. It has been suggested that metal may facilitate adsorption of the
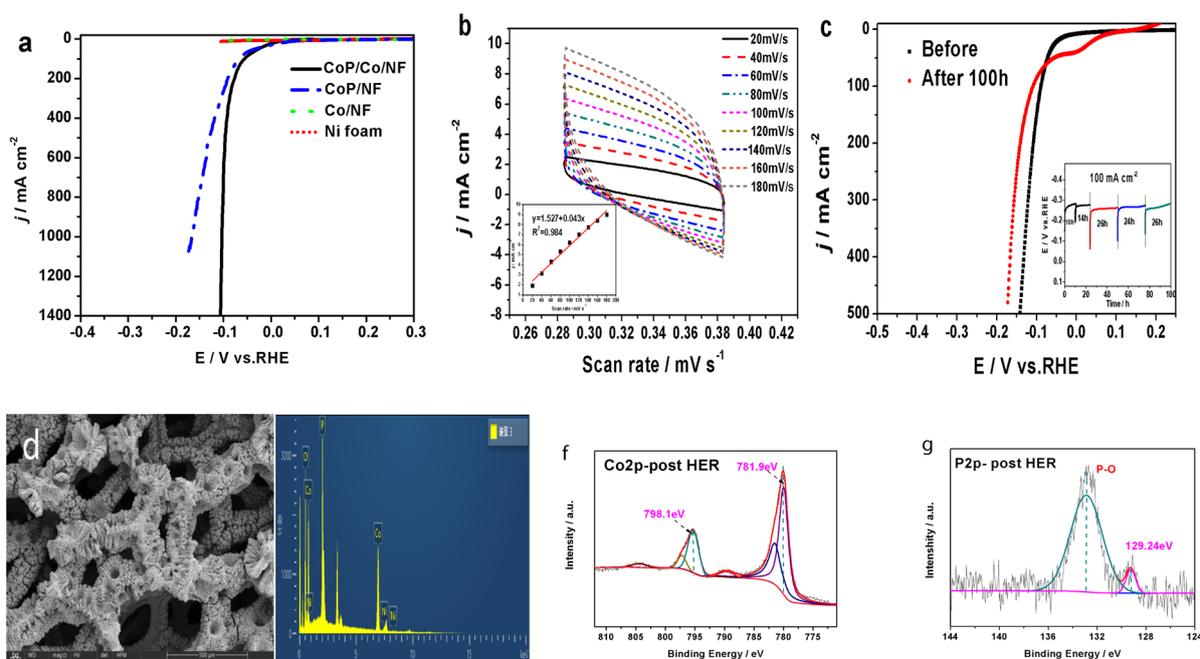

Fig. 8 (a) LSV hydrogen evolution polarization curves of the optimized CoP/Co/NF, CoP/NF, Co/NF and Ni foam; (b) cyclic voltammetry curves at different scan rate of 20–180 mV s^{-1} and relationship between scanning speed and current density of the CoP/Co/NF. (c) Polarization curves of CoP/Co/NF before and after HER at $J = -100$ mA cm^{-2} for 100 h, scanning rate: 2 mV s^{-1}, the insets shows chronopotentiometric curve of CoP/Co/NF; (d and e) SEM images and the corresponding EDX elemental mapping of CoP/Co on the Ni foam; (f and g) high-resolution XPS spectra of Co 2p and P 2p for the CoP/Co/NF after HER at 100 mA cm^{-2} for 100 h.

produced atomic hydrogen and its subsequent association to form H_2 from these intermediates. But it is generally inefficient in the water dissociation. Metal phosphoride may provide the active sites for dissociation of water. The combination of a metal Co and metal phosporide (CoP) may improve the kinetic rate of the HER in alkaline media.

3.2.3 CoP-nanorod/Co/NF catalytic performance for HER.
Fig. 8a shows the HER polarization curves with 75% online compensation of the optimized CoP/Co/NF, together with CoP/NF, Co/NF and nickel Foam electrodes in 1.0 M kOH electrolyte. The composite CoP/Co/NF catalysts showed higher HER activity than those of other referenced samples, suggesting significantly improved performance by incorporating CoP into metallic Co system and the synergistic interaction between metallic Co and CoP with hierarchical interfaces. The CoP/Co/NF catalyst electrode exhibits a lower over-potential (η) of 23 mV to reach current density of 10 mA cm^{-2} with the Tafel slope of 27.1 mV dec^{-1}. The electrode requires the η of 56 and 103 mV to produce high current densities of 100 and 1000 mA cm^{-2}. The composite electrode exhibited superior catalytic activity for HER to many reported CoP/NF based samples.[29,30] The catalytic performance of the prepared CoP/Co/NF is very close to the reported commercial Pt/C/NF (a η of 28 mV at 10 mA cm^{-2} and Tafel slope of 38 mV dec^{-1}), indicating an excellent HER kinetics of the composite catalyst in 1.0 M KOH.[21] The double layer capacitance (C_{dl}) of the electrode is calculated to be 21.5 mF cm$_{geo}^{-2}$ from the CV curves shown in Fig. 8b. The electrochemical active surface area (ECSA) is calculated by the formula ECSA = C_{dl}/C_s, C_s is generally taken as 40 μF cm^{-2} for transition metal phosphides.[27] so the ECSA of the catalyst electrode is obtained 537.5 cm^2, which is superior to the water electrolysis hydrogen evolution catalysts previously reported cobalt-based phosphides in the literature.[21–23] The higher C_{dl} and ECSA indicate that more active sites can be effectively utilized. It should be noted that the formula for ECSA calculation, ECSA = C_{dl}/C_s, is highly dependent on C_s. The surface electronic structures, ionic properties, and solvation characteristics of different materials may vary significantly. Turnover frequency (TOF) refers to the number of hydrogen molecules generated at a single active site per unit of time under a given over potential, which is used to reflect the intrinsic HER activity of catalysts. The TOF of CoP/Co/NF reaches 4.26 s^{-1} at an overpotential of

100 mV in 1 M KOH on the basis of ECSA values, which is comparable to the reported TOF data in the literature.[28–30] It should be mentioned that the exactly identifying the number of active sites remains challenging, giving rise to a tough exploration of the intrinsic activity of catalysts.[31,32] The reproducibility of a composite electrode evaluated by three repetitive measurements of the Tafel slope gave an R.S.D of 18.12%. These experiment data show a good reproducibility of CoP/Co/NF.

The stability of the catalyst-modified electrode is also an important factor for practical application. The long term stability of the electrode was tested by galvanostatic technique in a three-electrode system, with 1.0 M KOH as the electrolyte and a current density of −100 mA cm^{-2} for 100 h. As shown in Fig. 8c, the electrode exhibited an overpotential of approximately −256 mV to sustain a current density of −100 mA cm^{-2}, which remained almost unchanged after HER for 100 h. The hydrogen evolution overpotential decreased slightly, but the change was not significant, indicating that the hydrogen evolution stability of CoP/Co/NF was good. The SEM image and EDS mapping of the test CoP/Co/NF catalytic electrode in Fig. 8d and c show no significant morphological change and composition after HER for 100 h. The EDS elemental mapping of CoP/Co/NF shows a Co/P mole ratio of 2∶1 with the at% value of 36.86% Co, 18.13% P, 1.95% Ni and 43.06% O, which is consistent with the initial molecular structure of CoP/Co/NF (Co/P value of 1.8∶1) before electrolysis. The post-HER XPS of Co 2p and P 2p Fig. 8f and g exhibit no significant change for the composition and electronic structure of cobalt and phosphorous. The existence of the spin–orbit peak at 129.8 eV ascribed to P 2p$_{3/2}$ (M–P bond) illustrate the Co–P bond remain largely intact after 100 h HER, indicating the composite CoP/Co/NF has a good enduring stability under alkaline condition. Table 1 listed the comparison of the performance of the prepared CoP/Co/NF with the reported catalysts in recent references.

3.3 DFT calculations

To further reveal the interfacial synergistic effect between CoP nanorod and metallic Co and the interfacial charge distribution, DFT calculations were carried out. The geometrically optimized configurations of CoP, CoP/Co and CoP-O/Co (with a partially oxidized surface) are shown in Fig. 9a For HER in an alkaline electrolyte, a water molecule is first adsorbed onto the

Table 1 Comparison of the performance of the prepared CoP/Co/NF with the reported catalyst in recent references

Materials	η (mV) (10 mA cm^{-2})	η (mV) (100 mA cm^{-2})	Tafel slop (mV dec^{-1})	C_{dl} (mF cm^{-2})	References
Fe-CoP/NF	66	151	48.34	—	**15**
CoP/Ni$_2$P/NF	67.4	139.2	73.9	—	17
NiCo-hydroxide/Ni	93	—	116.7	—	24
Pt@NiFc-MOF	—	71	21	17.3	**33**
Ni$_3$N/Co$_2$N	35	111	34	23.2	34
Ru-based	13	60	30	—	35
NiS-Ni$_2$P/Ni/NF	53	139	44.3	60.9	22
Ni$_{76}$Mo$_{20}$W$_4$	354	556	87.6	2.96	36
NiFeO/NiMoO/NF	46	178	85	24.08	37
CoP/Co/NF	**23**	**56**	**27.1**	**21.5**	**This work**

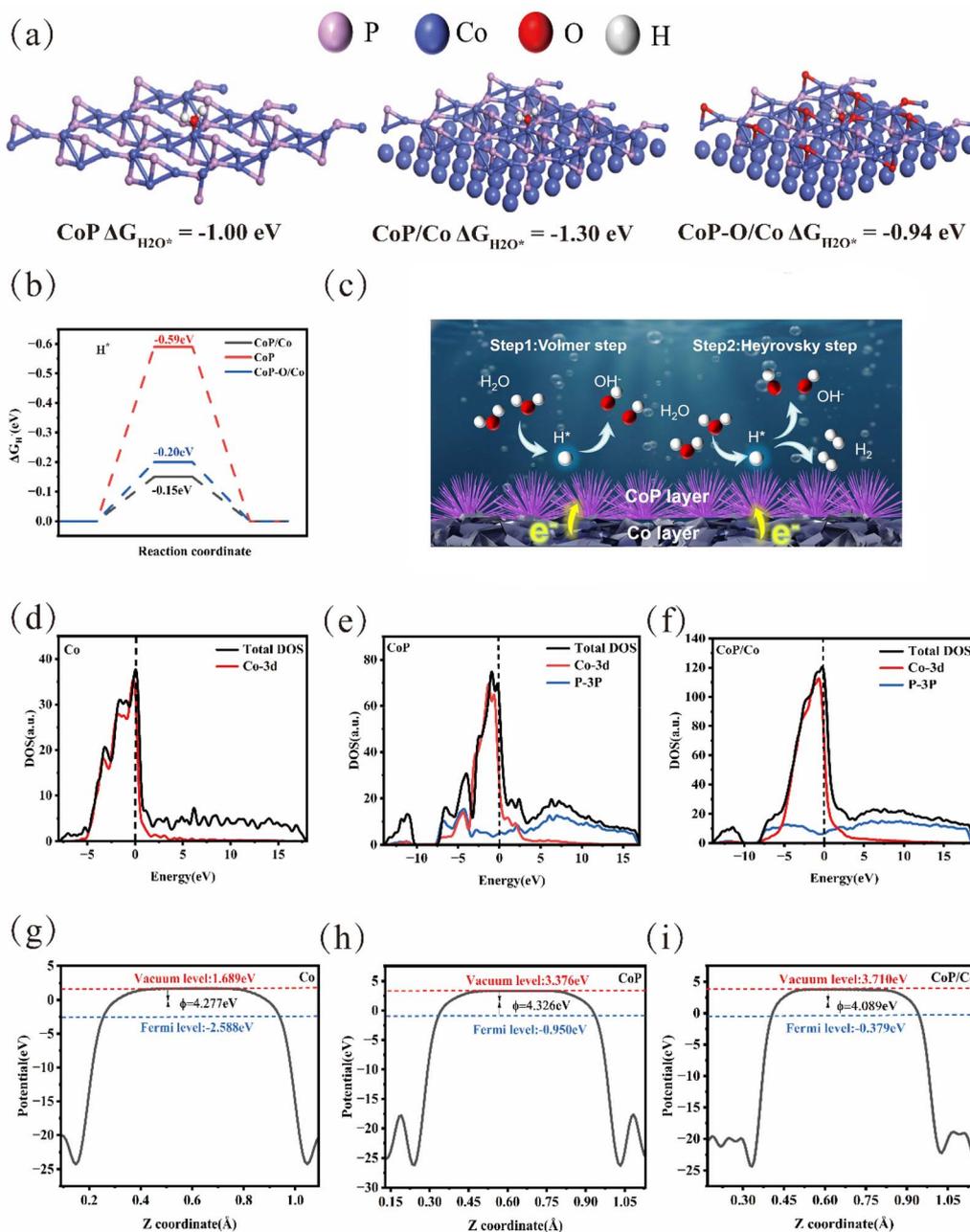© 2026 The Author(s). Published by the Royal Society of Chemistry

Fig. 9 (a) Schematic diagram of H_2O molecule adsorption on CoP, CoP/Co and CoP–O/Co surfaces; (b) free energy diagram of H adsorption on CoP/Co, CoP amd CoP–O. (c) Schematic diagram of HER on CoP/Co/NF; (d–f) TDOS and PDOS calculation for Co, CoP and CoP/Co; (g–i) WF of Co, CoP, and CoP/Co.

catalytic active site to form H_2O^*, and then undergoes two kinetic steps: (A) the H_2O dissociation step (Volmer step) producing H^* and OH^-, and (B) the H_2 formation stage (Heyrovsky or Tafel step). The rate of alkaline HER is determined by the significant kinetic barriers associated with both the water dissociation and hydrogen generation stages. HER efficiency under alkaline conditions is also strongly influenced by H_2O^* due to the fact that poor adsorption capability for H_2O leads to a scarce source of H_2O for the Volmer reaction.[16] Therefore, the water molecule adsorption capabilities of CoP, CoP/Co and CoP–

O/Co were evaluated using $\Delta G_{H_2O^*}$. The calculated $\Delta G_{H_2O^*}$ of CoP/Co (-1.30 eV) shows more negative than those of the $\Delta G_{H_2O^*}$ of CoP–O/Co (-0.94 eV) and CoP (-1.00 eV), indicating a stronger charge interaction with water molecules on the CoP/Co surface. This implies that the CoP/Co surface can effectively promote the adsorption of water molecules. It is worth mentioning that the adsorption effect of CoP–O/Co is reduced due to its partially oxidized surface.

A ΔG_{H^*} value close to zero is considered the optimal condition for HER, meaning the adsorption strength of H^* is neither

too strong nor too weak.[38] The ΔG_{H*} (shown in Fig. 9b) for the CoP/Co is −0.15 eV, very close to thermodynamic neutrality, indicating that the CoP/Co surface possesses favorable H* adsorption and desorption capabilities. The ΔG_{H*} values for partially oxidized CoP-O/Co and single CoP are −0.20 eV and −0.59 eV, respectively, suggesting that the oxidized CoP-O/Co and single CoP surfaces have weaker H adsorption capabilities, leading to more difficult for the H* formation. Importantly, the density of states (DOS) calculations results in Fig. 9d–f shows the highest total density of states (TDOS) of the CoP/Co near the Fermi level due to the introduction of metallic Co sites, compared with that of the single Co and CoP. The results indicate that CoP/Co has more electronic states than single CoP, which demonstrates that the introduction of metallic Co enhances the electronic conductivity of the catalyst, endowing it with stronger catalytic capability. The highest TDOS means the significant hybridization between the Co 3d and P 3p orbitals, indicating strong electronic interaction and a synergistic effect between Co and P, which contributes to the highly efficient HER activity of the CoP/Co catalyst.

The work function (WF) value may exhibit the direction and feasibility of electron transfer.[39,40] As shown in Fig. 9g–i, the WF of CoP/Co, CoP and Co are 4.089 eV, 4.326 eV, and 4.277 eV, respectively. This further reflects the optimization of the interfacial structure after introducing CoP, which attracts electrons from Co to CoP and reduces the energy barrier for the hydrogen evolution reaction. Based on the theoretical calculations, the fundamental HER mechanism on the CoP/Co surface can be illustrated in Fig. 9c. By introducing the metallic Co as an "electron pump" into the CoP system, the CoP/Co heterostructure exhibits excellent hydrogen adsorption and desorption capabilities, the lower water dissociation energy barrier, thus improving the efficiency of the HER process. Studies have shown that when a metal Co and a semiconductor CoP come into contact, if their Fermi levels differ, electrons will spontaneously flow across the interface until the Fermi levels equilibrate. This electron flow creates a space charge region at the interface, generating a built-in electric field (BIEF). BIEF can cause the bending of the energy bands on the semiconductor side, thereby altering the electron density and d-band center positions of the surface active sites. BIEF can accelerate electron transfer from the electrode to the active sites while polarizing water molecules adsorbed on the surface, making them more prone to dissociation.

4 Conclusions

The high-performance hetero-structured electrocatalyst of CoP nanorods doped with metallic Co on nickel foam was designed *via* a facile electrodeposition followed by a controlled low-temperature phosphorization strategy. The electrode has a nanoporous sea-urchin-like arrays with a large electrochemical surface area, which is beneficial to the rapid transfer of charges and gas bubble detachment. By introducing the metallic Co as an "electron pump" into the CoP system, donating electrons to the CoP phase to enhance intrinsic conductivity, the CoP/Co heterostructure exhibits excellent

hydrogen adsorption and desorption capabilities, the lower water dissociation energy barrier, thus improving the efficiency of the HER process. The electrode has high catalytic activity for the water electrolysis hydrogen evolution reaction in 1.0 M KOH electrolyte. The overpotential is 56 and 103 mV at a high current density of 100 and 1000 mA cm^{-2}, and the Tafel slope is 27.1 mV dec^{-1}. After 100 h of galvanostatic HER at 100 mA cm^{-2}, the electrode shows high stability and has considerable practical application prospect.

Author contributions

Yuanze Wei: methodology, experimental data production, analysis of the obtained results and preparation of manuscript materials. Shiyu Yang: experimental data production, analysis of the obtained results and conceptualization. Danyang Yu: generalization of the obtained results and writing of the original manuscript. Zhifan Xue: conceptualization, discussion of results, manuscript editing and guidance. Benxue Zou: methodology and analysis.

Conflicts of interest

There are no conflicts of interest to declare.

Note added after first publication

This article replaces the version published on 13 February 2026, which included incorrect versions of Fig. 1 and 9c.

Data availability

The authors confirm that all data supporting this study have been included in the article.

Acknowledgements

Notes and references

1 S. H. Osman, N. S. M. Yatim, O. S. J. Elham, N. Shaari and Z. Zakaria, *Sustain. Energy Fuels*, 2025, **9**, 3182–3202.
2 S. O. Akpasi, I. M. S. Anekwe, E. K. Tetteh, U. O. Amune, S. I. Mustapha and S. L. Kiambi, *Clean Energy*, 2025, **9**(1), 52–88.
3 J. J. Shi, Y. Bao, R. Ye, Ju Zhong, L. Zhou, Z. Zhao, W. Kang and S. B. Aidarova, *Catal. Sci. Technol.*, 2025, **15**, 2104–2131.
4 Y. Yang, C. R. Peltier, R. Zeng, R. Schimmenti and H. D. Abruña, *Chem. Rev.*, 2022, **122**(6), 6117–6321.
5 H. Tüysüz, *Acc. Chem. Res.*, 2024, **57**(4), 558–567.
6 A. R. Fairhurst, J. Snyder, C. Wang, D. Strmcnik and V. R. Stamenkovic, *Chem. Rev.*, 2025, **125**(3), 1332–1419.

7 H. Xiong, R. Zhuang, B. Cheng, D. Liu, Y. Du, H. Wang, Y. Liu, F. Xu and H. Wang, *Adv. Energy Mater.*, 2025, **15**, 2404077.

8 T. D. Mai and H. H. Do, *Tungsten*, 2024, **6**, 488–503.

9 Z. W. Seh, J. Kibsgaard, C. F. Dickens, I. B. Chorkendorff, J. K. Nørskov and T. F. Jaramillo, *Science*, 2017, **355**, eaad4998.

10 W. Liu, M. Zhou, J. Zhang, W. Liu, D. Qin, Q. Liu, G. Hu and X. Liu, *Mater. Chem. Front.*, 2025, **9**, 953–964.

11 A. V. Munde, B. B. Mulik, R. P. Digholea and B. R. Sathe, *New J. Chem.*, 2020, **44**, 15776–15784.

12 R. V. Digraskar, V. S. Sapner, S. S. Narwade, S. M. Mali, A. V. Ghuleb and B. R. Sathe, *RSC Adv.*, 2018, **8**, 20341–20346.

13 P. K. Bhoja, R. A. Chavana, S. A. Manea, D. M. Ulissoa, J. Heob, I. W. P. Chenc, J. B. Yadavd, T. D. Dongalee, B. R. Sathef and A. V. Ghule, *Int. J. Hydrogen Energy*, 2024, **88**, 604–616.

14 Y. Xu, J. Du, J. Jiang, Y. Miao, Z. Zhuang, Z. Liu, Y. Yan, R. Pan, J. Yang, M. Wang, S. Gu, L. Kang and D. Wang, *Angew. Chem.*, 2025, **64**, e202502227.

15 S. Liu, F. Meng, B. Wang, Y. Feng and Z. Du, *J. Electroanal. Chem.*, 2025, **987**, 119116.

16 Y. Liu, L. Wang, R. Hübner, J. Kresse, X. Zhang, M. Deconinick, Y. Vaynzof, I. M. Weidinger and A. Eychmüller, *Angew. Chem.*, 2024, **36**, e202319239.

17 X. Wang, X. Xiao, C. Chen, J. Hu, L. Zhang, D. Sun and X. Xu, *Chem. Eng. Sci.*, 2025, **301**, 120740.

18 C. Liu, L. Yu, N. Chen, G. Tian and H. Zhu, *Inorg. Chem. Front.*, 2025, **12**, 2058–2069.

19 R. Fürstner, W. Barthlott, C. Neinhuis and P. Walzel, *Langmuir*, 2005, **21**(3), 956–961.

20 S. Banerjee, D. D. Dionysiou and S. C. Pillai, *Appl. Catal. B Environ.*, 2015, **176**, 396–428.

21 Y. Lu, W. Li, J. He, W. Zhang, J. Hu, T. Wu, D. Zhou and W. Hu, *J. Alloys Compd.*, 2025, **1030**, 180847.

22 M. Liu, Z. Sun, C. Zhang, S. Li, C. He, Y. Liu and Z. Zhao, *J. Mater. Chem. A*, 2022, **10**, 13410–13417.

23 B. Zhang, S. Zhou, Y. Yao, H. Jiang, J. Sui and B. Zou, *ChemistrySelect*, 2023, **8**(41), e202301672.

24 Y. Sun, S. Zhou, N. Yang, H. Shen, X. Yang, L. Zhang, X. Xiao, B. Jiang and L. Zhang, *J. Colloid Interface Sci.*, 2025, **688**, 1–10.

25 W. Liu, M. Zhou, J. Zhang, W. Liu, D. Qin, Q. Liu, G. Hu and X. Liu, *Mater. Chem. Front.*, 2025, **9**, 953–964.

26 Y. Xiao, X. Chen, T. Li, Y. Mao, C. Liu, Y. Chena and W. Wang, *Int. J. Hydrogen Energy*, 2022, **47**, 9915–9924.

27 Hi Cao, Z. Li, Y. Xie, F. Xiao, H. Wang, X. Wang, K. Pan and A. Cabot, *ChemSusChem*, 2021, **14**, 1094–1102.

28 X. Huang, X. Xu, X. Luan and D. Cheng, *Nano Energy*, 2020, **68**, 104332.

29 W. Tan and H. He, *RSC Adv.*, 2025, **15**, 39355.

30 S. Anantharaj, S. R. Ede, K. Karthick, S. S Sankar, K. Sangeetha, P. E. Karthikc and S. Kundu, *Energy Environ. Sci.*, 2018, **11**, 744–771.

31 Y. Lu, W. Li, J. He, W. Zhang, J. Hu, T. Wu, D. Zhou and W. Hu, *J. Alloys Compd.*, 2025, **1030**, 180847.

32 L. Xiong, Y. Qiu, X. Peng, Z. Liu and P. K. Chu, *Nano Energy*, 2022, **104**, 107882.

33 Y. Huang, X. Zhang, L. Li, M. Humayun, H. Zhang, X. Xu, S. PAnthony, Z. Chen, J. Zeng, D. V. Shtansky, K. Huo, H. Song, C. Wang and W. Zhang, *Adv. Funct. Mater.*, 2025, **35**, 2401011.

34 Q. Hu, K. Gao, X. Wang, H. Zheng, J. Cao, L. Mi, Q. Huo, H. Yang, J. Liu and C. He, *Nat. Commun.*, 2022, **13**(1), 3958.

35 M. Liu, Z. Sun, C. Zhang, S. Li, C. He, Y. Liu and Z. Zhao, *J. Mater. Chem. A*, 2022, **10**, 13410–13417.

36 Y. An, W. Wu, L. Kong, Y. Jiao, X. Li, M. M. Yusif and Q. Wang, *Fuel*, 2026, **409**, 137915.

37 Y. Shen, P. Wu, C. Wang, W. Yuan, W. Yang and X. Shang, *Int. J. Hydrogen Energy*, 2023, **48**(85), 33130–33138.

38 N. Wang, Y. Zhang, C. Zhang, X. Wang, S. Dai, M. Huang and H. Jiang, *Chem. Commun.*, 2025, **61**, 3191–3194.

39 Y. Wen, J. Qi, P. Wei, X. Kanga and X. Li, *J. Mater. Chem. A*, 2021, **9**, 10260–10269.

40 G. E. O Nsang, B. Ullah, S. Hua, S. A. Shah, N. Ullah, N. Ullah, F. N. Dike, W. Yaseen, A. Yuan, N. Khan and H. Ullah, *Energy Storage Mater.*, 2025, **5**, 50047.